Journal of Theoretical and Applied Physics
a SpringerOpen Journal

RESEARCH Open Access

Calculation of full-energy peak efficiency of NaI (Tl) detectors by new analytical approach for parallelepiped sources

Ahmed M El-Khatib[1], Mohamed S Badawi[1*], Mona M Gouda[1], Slobodan I Jovanovic[2,3], Aleksandar D Dlabac[3], Nikola N Mihaljevic[3,4], Sherif S Nafee[1] and Ekram A El-Mallah[1]

Abstract

A new analytical approach is presented for the calculation of full-energy peak (FEP) efficiency of NaI (Tl) detectors. The self-attenuation of the parallelepiped source matrix, the attenuation by the source container, and the detector housing materials were considered in the mathematical treatment. The efficiency values calculated using the presently suggested analytical approach are compared with those measured values obtained by two different sizes of NaI (Tl) detectors. The calculated and the measured full-energy peak efficiency values were in a good agreement.

Keywords: NaI (Tl) scintillation detectors; Parallelepiped sources; Full-energy peak efficiency; Self-attenuation

Introduction

One of the most important parameters in the calculation of the gamma activity of environmental radioactive sources with respect to emitted gamma energy is the detection efficiency which is usually determined using calibrated standard sources [1]. Standard radioactive sources, if available, are costly and would need to be renewed, especially when the radionuclides have short half-lives [2]. In addition to the influence of the source matrix on the counting efficiency which can be expressed by the self-attenuation factor, the fraction of the gamma rays not registered in the full-energy peak is due to the scattering or absorption within the sample [3]. An effective tool to overcome these problems could be the use of computational techniques [4-9] to complete the calibration of the gamma spectrometry system. Also, Selim and Abbas [10-14] solved these problems by deriving direct analytical integrals of the detector efficiencies (total- and full-energy peak) for any source-detector configuration and implemented these analytical expressions into a numerical integration computer program. Moreover, they [15-18] introduced a new theoretical approach based on that direct statistical method to determine the detector efficiency for an isotropic radiating point source at any arbitrary position from a cylindrical detector, as well as the extension of this approach to evaluate the volumetric sources.

In a large extent, we introduced a new analytical approach for the calculation of full-energy peak efficiency of the coaxial detector with respect to point and volumetric sources (cylindrical and spherical) [19-21]. In the present work, we deal with parallelepiped source. The basic idea of this approach is the separate calculation of the intrinsic and the geometrical efficiencies, and the factors which related to the photon attenuation in the detector end cap, inactive layer, source container, and the self-attenuation of the source matrix. The calculations depend on two main factors. First is the accurate analytical calculation of the average path length covered by the photon in each of the following: the detector active volume, the source matrix, the source container, the inactive layer, and the end cap of the detector. Second is the geometrical solid angle Ω.

Basics of the efficiency computation

The case of a non-axial point source

Consider a right circular cylindrical ($2R \times L$) detector and an arbitrarily positioned isotropic point source located at a distance h from the detector top surface and at a lateral distance ρ from its axis, as shown in Figure 1.

* Correspondence: ms241178@hotmail.com
[1]Physics Department, Faculty of Science, Alexandria University, Alexandria 21511, Egypt
Full list of author information is available at the end of the article

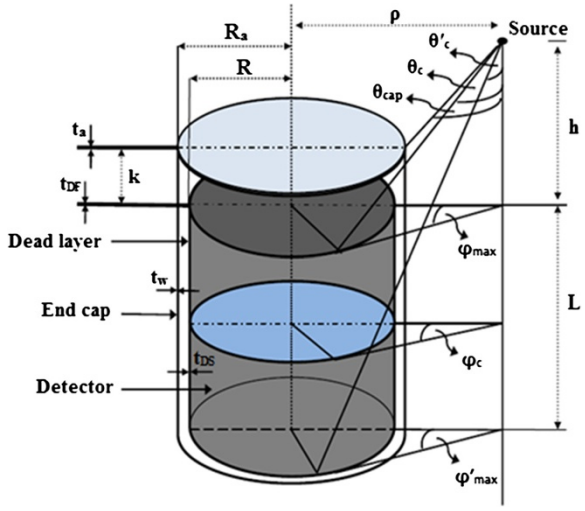

Figure 1 A diagram of a cylindrical-type detector with a non-axial point source ($\rho > R$).

The efficiency of the detector with respect to point source is given as follows [16]:

$$\varepsilon_{\text{point}} = f_{\text{att}}\,\varepsilon_{\text{g}}\,\varepsilon_{\text{i}}, \tag{1}$$

where ε_{i} and ε_{g} are the intrinsic and the geometrical efficiencies which are derived by Abbas et al. [16]. f_{att} is the attenuation factor of the detector inactive layer and end cap material. In 'The attenuation factor (f_{att})' section, this factor will be recalculated by a new method.

The intrinsic (ε_i) and the geometrical (ε_g) efficiencies

The intrinsic and geometrical efficiencies are represented by Equations 2 and 3, respectively.

$$\varepsilon_{\text{i}} = 1 - e^{-\mu \bar{d}} \tag{2}$$

$$\varepsilon_{\text{g}} = \frac{\Omega}{4\pi}, \tag{3}$$

where μ is the attenuation coefficient of the detector material. $\bar{d}$ is the average path length traveled by a photon through the detector, and Ω is the solid angle subtended by the source-detector; they are represented by Equations 4 and 5, respectively. These will be discussed in detail according to the source-detector configuration as shown below:

$$\bar{d} = \frac{\int_{\Omega} d(\theta,\varphi)\, d\Omega}{\int_{\Omega} d\Omega} = \frac{\int_{\varphi}\int_{\theta} d(\theta,\varphi)\sin\theta d\theta d\varphi}{\Omega}, \tag{4}$$

where θ and φ are the polar and the azimuthal angles, respectively. $d\ (\theta,\varphi)$ is the possible path length traveled by the photon within the detector active volume.

$$\Omega = \int_{\varphi}\int_{\theta} \sin\theta\, d\theta\, d\varphi. \tag{5}$$

There are two main cases to be considered for calculating the intrinsic and geometrical efficiencies of the detector with respect to point source, namely, (1) the lateral displacement of the source is smaller than or equal the detector circular face's radius ($\rho \le R$), and (2) the lateral distance of the source is greater than the detector circular face's radius ($\rho > R$). The two cases have been treated by Abbas et al. [16]. The values of the polar and the azimuthal angles based on the source-to-detector configuration are shown in Table 1.

The attenuation factor (f_{att})

The attenuation factor f_{att} is expressed as:

$$f_{\text{att}} = f_{\text{lay}}\, f_{\text{cap}}, \tag{6}$$

where f_{lay} and f_{cap} are the attenuation factors of the detector inactive layer and end cap material, respectively, and they are given by:

$$f_{\text{lay}} = e^{-\mu_{\text{lay}}\ \overline{\delta_{\text{lay}}}} \quad , \quad f_{\text{cap}} = e^{-\mu_{\text{cap}}\ \overline{\delta_{\text{cap}}}}, \tag{7}$$

where μ_{lay} and μ_{cap} are the attenuation coefficients of the detector inactive layer and end cap material, respectively. $\bar{\delta}_{\text{lay}}$ and $\bar{\delta}_{\text{cap}}$ are the average path length traveled by a photon through the detector inactive layer and the end cap material, respectively, and they are represented as follows:

$$\overline{\delta_{\text{lay}}} = \frac{\int_{\varphi}\int_{\theta} t'(\theta,\varphi)\sin\theta\, d\theta\, d\varphi}{\int_{\varphi}\int_{\theta} \sin\theta\, d\theta\, d\varphi} = \frac{\int_{\varphi}\int_{\theta} t'(\theta,\varphi)\sin\theta\, d\theta\, d\varphi}{\Omega}$$
$$\overline{\delta_{\text{cap}}} = \frac{\int_{\varphi}\int_{\theta} t''(\theta,\varphi)\sin\theta\, d\theta\, d\varphi}{\int_{\varphi}\int_{\theta} \sin\theta\, d\theta\, d\varphi} = \frac{\int_{\varphi}\int_{\theta} t''(\theta,\varphi)\sin\theta\, d\theta\, d\varphi}{\Omega}, \tag{8}$$

where $t'(\theta,\varphi)$ and $t''(\theta,\varphi)$ are the possible path lengths traveled by the photon within the detector inactive layer and the end cap material, respectively.

Consider that the detector has an inactive layer covering its upper surface with thickness t_{DF} and its side surface with thickness t_{DS}, as shown in Figure 1. The possible path lengths and the average path length traveled by the photon within the inactive layer for cases ($\rho \le R$) and ($\rho > R$) are shown in Table 2, where t'_1 and t'_2 represent the photon path length through the upper and the side surface of the inactive layer, respectively.

Consider that the thickness of the upper and side surfaces of the detector end cap material is t_{a} and t_{w}, respectively, as shown in Figure 1. The possible path

Table 1 The values of the polar and the azimuthal angles based on the source-to-detector configuration [16]

The polar angles	The azimuthal angles
$\theta_1 = \tan^{-1}\left(\frac{\lvert R-\rho\rvert}{h+L}\right)$	$\varphi_{\max} = \cos^{-1}\left(\frac{\rho^2-R^2+h^2\tan^2\theta}{2\rho h\tan\theta}\right)$
$\theta_2 = \tan^{-1}\left(\frac{\lvert R-\rho\rvert}{h}\right)$	$\varphi'_{\max} = \cos^{-1}\left(\frac{\rho^2-R^2+(h+L)^2\tan^2\theta}{2\rho(h+L)\tan\theta}\right)$
$\theta_3 = \tan^{-1}\left(\frac{R+\rho}{h+L}\right)$	
$\theta_4 = \tan^{-1}\left(\frac{R+\rho}{h}\right)$	
$\theta_c = \tan^{-1}\left(\frac{\sqrt{\rho^2-R^2}}{h+L}\right)$	
$\theta_c' = \tan^{-1}\left(\frac{\sqrt{\rho^2-R^2}}{h}\right)$	$\varphi_c = \sin^{-1}\left(\frac{R}{\rho}\right)$
$\theta_T = \tan^{-1}\left(\frac{\sqrt{\rho^2-R^2}}{\sqrt{h(h+L)}}\right)$ $(\varphi_{\max} = \varphi'_{\max})$	

lengths and the average path length traveled by the photon within the detector end cap material for cases ($\rho \le R$) and ($\rho > R$) are shown in Table 3, where t''_1 and t''_2 represent the photon path length through the upper and the side surface of the detector end cap material, respectively. From Table 3, it was observed that the case in which ($\rho > R$) has two sub-cases which are ($R < \rho \le R_a$) and ($\rho > R_a$), where R_a is the inner radius of the detector end cap. There is a very important polar angle (θ_{cap}) which must be considered when we study the case in which $\rho > R_a$, and this is given by the equation below:

$$\theta_{cap} = \tan^{-1}\left(\frac{\rho - R_a}{h-k}\right), \tag{9}$$

where k is the distance between the detector end cap and the detector upper surface.

The case of a parallelepiped (block) source

Consider a block source with dimensions A (major side), B (minor side), and H (height) as illustrated in Figure 2, then the efficiency is given by the equation below:

Table 2 Possible path lengths and their average traveled by the photon within the inactive layer [$\rho \le R$ and $\rho > R$]

$\rho \le R$	$\rho > R$
$t'_1 = \frac{t_{DF}}{\cos\theta}$	$t'_1 = \frac{t_{DF}}{\cos\theta}$
	$t'_2 = \frac{\rho\cos\varphi + \sqrt{(R+t_{DS})^2-\rho^2\sin^2\varphi}}{\sin\theta} - \frac{\rho\cos\varphi + \sqrt{(R)^2-\rho^2\sin^2\varphi}}{\sin\theta} \cong \frac{t_{DS}\left(1+\frac{\rho^2}{2R^2}\sin^2\varphi\right)}{\sin\theta}$
$\overline{\delta_{lay}} = \frac{Z_1}{I_2}$	$\overline{\delta_{lay}} = \frac{Z_3}{I_4}$
$Z_1 = \int_0^{\pi}\int_0^{\theta_2} t'_1 \sin\theta\, d\theta\, d\varphi + \int_0^{\varphi_{\max}}\int_{\theta_2}^{\theta_4} t'_1 \sin\theta\, d\theta\, d\varphi$	$Z_3 = \int_{\theta_1}^{\theta_2}\int_0^{\varphi'_{\max}} t'_2 \sin\theta\, d\varphi\, d\theta + \int_{\theta_2}^{\theta'_c}\int_0^{\varphi'_{\max}} t'_1 \sin\theta\, d\varphi\, d\theta + \int_{\theta'_c}^{\theta_c}\int_0^{\varphi_c} t'_1 \sin\theta\, d\varphi\, d\theta + \int_{\theta_c}^{\theta_4}\int_0^{\varphi_{\max}} t'_1 \sin\theta\, d\varphi\, d\theta$, $(\theta_2 \ge \theta'_c)$
	$Z_3 = \int_{\theta_1}^{\theta'_c}\int_0^{\varphi'_{\max}} t'_2 \sin\theta\, d\varphi\, d\theta + \int_{\theta'_c}^{\theta_2}\int_0^{\varphi_c} t'_2 \sin\theta\, d\varphi\, d\theta + \int_{\theta_2}^{\theta_c}\int_0^{\varphi_c} t'_1 \sin\theta\, d\varphi\, d\theta + \int_{\theta_c}^{\theta_4}\int_0^{\varphi_{\max}} t'_1 \sin\theta\, d\varphi\, d\theta$, $(\theta_2 < \theta_c)$

Table 3 Possible path lengths and their average traveled by the photon within the detector end cap [$\rho \le R$ and $\rho > R$]

$\rho \le R$	$\rho > R$	
	$R < \rho \le R_a$	$\rho > R_a$
$t''_1 = \frac{t_a}{\cos\theta}$	$t''_1 = \frac{t_a}{\cos\theta}$	$t''_1 = \frac{t_a}{\cos\theta}$ $t''_2 = \frac{\rho\cos\varphi + \sqrt{(R_a + t_w)^2 - \rho^2\sin^2\varphi}}{\sin\theta} - \frac{\rho\cos\varphi + \sqrt{(R_a)^2 - \rho^2\sin^2\varphi}}{\sin\theta} \cong \frac{t_w\left(1 + \frac{\rho^2}{2R_a{}^2}\sin^2\varphi\right)}{\sin\theta}$
$\overline{\delta_{cap}} = \frac{Z'_1}{l_2}$	$\overline{\delta_{cap}} = \frac{Z'_3}{l_4}$	$\overline{\delta_{cap}} = \frac{Z'_3}{l_4}$
$Z'_1 = \int_0^{\pi\theta_2}\int_0^{} t''_1 \sin\theta\, d\theta\, d\varphi + \int_0^{\varphi_{max}}\int_{\theta_2}^{\theta_4} t''_1 \sin\theta\, d\theta\, d\varphi$	$Z'_3 = \int_{\theta_1}^{\theta'_c}\int_0^{\varphi'_{max}} t''_1 \sin\theta\, d\varphi\, d\theta + \int_{\theta'_c}^{\theta_c}\int_0^{\varphi_c} t''_1 \sin\theta\, d\varphi\, d\theta + \int_{\theta_c}^{\theta_4}\int_0^{\varphi_{max}} t''_1 \sin\theta\, d\varphi\, d\theta$	$Z'_3 = \int_{\theta_1}^{\theta'_c}\int_0^{\varphi'_{max}} t''_1 \sin\theta\, d\varphi\, d\theta + \int_{\theta'_c}^{\theta_c}\int_0^{\varphi_c} t''_1 \sin\theta\, d\varphi\, d\theta + \int_{\theta_c}^{\theta_4}\int_0^{\varphi_{max}} t''_1 \sin\theta\, d\varphi\, d\theta$ $\theta_1 \ge \theta_{cap}$
		$Z'_3 = \int_{\theta_1}^{\theta_{cap}}\int_0^{\varphi'_{max}} t''_2 \sin\theta\, d\varphi\, d\theta + \int_{\theta_{cap}}^{\theta'_c}\int_0^{\varphi'_{max}} t''_1 \sin\theta\, d\varphi\, d\theta + \int_{\theta'_c}^{\theta_c}\int_0^{\varphi_c} t''_1 \sin\theta\, d\varphi\, d\theta + \int_{\theta_c}^{\theta_4}\int_0^{\varphi_{max}} t''_1 \sin\theta\, d\varphi\, d\theta$ $\theta'_c > \theta_{cap}$
		$Z'_3 = \int_{\theta_1}^{\theta'_c}\int_0^{\varphi'_{max}} t''_2 \sin\theta\, d\varphi\, d\theta + \int_{\theta'_c}^{\theta_{cap}}\int_0^{\varphi_c} t''_2 \sin\theta\, d\varphi\, d\theta + \int_{\theta_{cap}}^{\theta_c}\int_0^{\varphi_c} t''_1 \sin\theta\, d\varphi\, d\theta + \int_{\theta_c}^{\theta_4}\int_0^{\varphi_{max}} t''_1 \sin\theta\, d\varphi\, d\theta$ $\theta_{cap} \ge \theta'_c$
		$Z'_3 = \int_{\theta_1}^{\theta'_c}\int_0^{\varphi'_{max}} t''_2 \sin\theta\, d\varphi\, d\theta + \int_{\theta'_c}^{\theta_c}\int_0^{\varphi_c} t''_2 \sin\theta\, d\varphi\, d\theta + \int_{\theta_c}^{\theta_{cap}}\int_0^{\varphi_{max}} t''_2 \sin\theta\, d\varphi\, d\theta + \int_{\theta_{cap}}^{\theta_4}\int_0^{\varphi_{max}} t''_1 \sin\theta\, d\varphi\, d\theta$ $\theta_4 > \theta_{cap} \ge \theta_c$
		$Z'_3 = \int_{\theta_1}^{\theta'_c}\int_0^{\varphi'_{max}} t''_2 \sin\theta\, d\varphi\, d\theta + \int_{\theta'_c}^{\theta_c}\int_0^{\varphi_c} t''_2 \sin\theta\, d\varphi\, d\theta + \int_{\theta_c}^{\theta_4}\int_0^{\varphi_{max}} t''_2 \sin\theta\, d\varphi\, d\theta$ $\theta_{cap} \ge \theta_4$

$$\varepsilon_{block} = \frac{4 S_{self} S_{sc} f_{att} \varepsilon_i \varepsilon_g}{V}, \tag{10}$$

where V is the volume of the block source ($V = ABH$), S_{self} is the self-attenuation factor of the source matrix, and S_{sc} is the attenuation factor of the source container material.

The intrinsic and geometrical efficiencies are defined before in Equations 2 and 3, respectively, but the average path length $\bar{d}$ traveled by the photon through the detector and the solid angle will have new forms due to the geometry of Figure 2. The average path length is expressed as follows:

$$\bar{d} = \frac{\int_{h_o}^{H+h_o}\left(\int_0^{\alpha_T} N_{b1}\, d\alpha + \int_{\alpha_T}^{\frac{\pi}{2}} N_{b2}\, d\alpha\right) dh}{\int_{h_o}^{H+h_o}\left(\int_0^{\alpha_T} N_{b3}\, d\alpha + \int_{\alpha_T}^{\frac{\pi}{2}} N_{b4}\, d\alpha\right) dh}. \tag{11}$$

The geometrical efficiency ε_g is given by

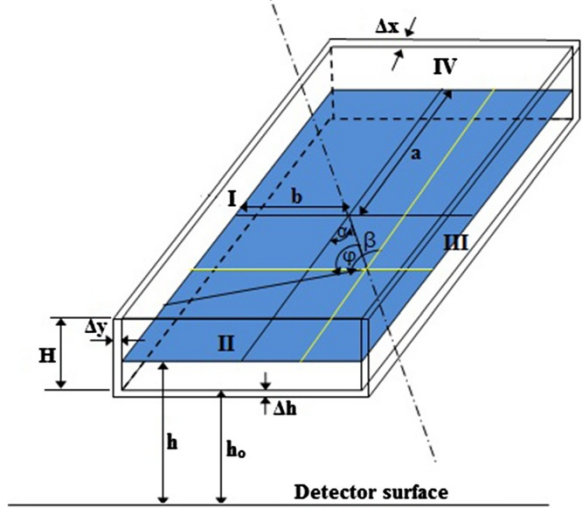

Figure 2 Schematic diagram of parallelepiped source.

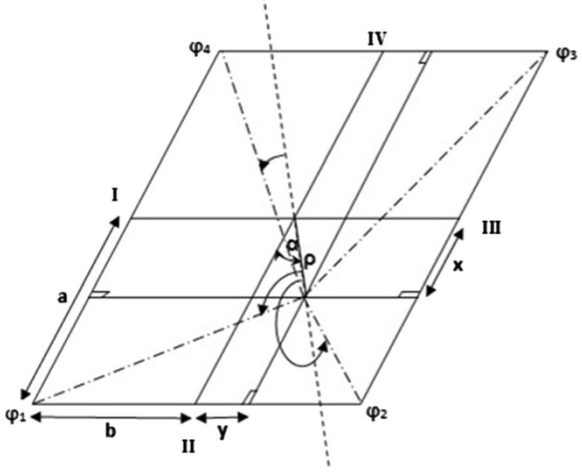

Figure 4 Schematic view for the azimuthal angle values in the bar source ($\alpha < \alpha_T$).

$$\varepsilon_g = \frac{\int_{h_o}^{H+h_o}\left(\int_0^{\alpha_T} N_{b3}\,d\alpha + \int_{\alpha_T}^{\frac{\pi}{2}} N_{b4}\,d\alpha\right)dh}{2\pi}, \tag{12}$$

where α is the angle between the lateral distance ρ and the detector's major axis, as shown in Figures 3 and 4. The factor 4 is introduced in Equation 10 to cover the values of α from 0 to 2π. The values of N_{b1}, N_{b2}, N_{b3}, and N_{b4} are given as follows:

$$N_{b1} = \begin{cases} \int_0^{\rho_1} I_1(\rho \le R)\ \rho\,d\rho & (\rho_1 \le R) \\ \int_0^{R} I_1(\rho \le R)\rho\,d\rho + \int_R^{\rho_1} I_1(\rho > R)\rho\,d\rho & (\rho_1 > R) \end{cases} \tag{13}$$

$$N_{b2} = \begin{cases} \int_0^{\rho_2} I_1(\rho \le R)\ \rho\,d\rho & (\rho_2 \le R) \\ \int_0^{R} I_1(\rho \le R)\rho\,d\rho + \int_R^{\rho_2} I_1(\rho > R)\rho\,d\rho & (\rho_2 > R) \end{cases} \tag{14}$$

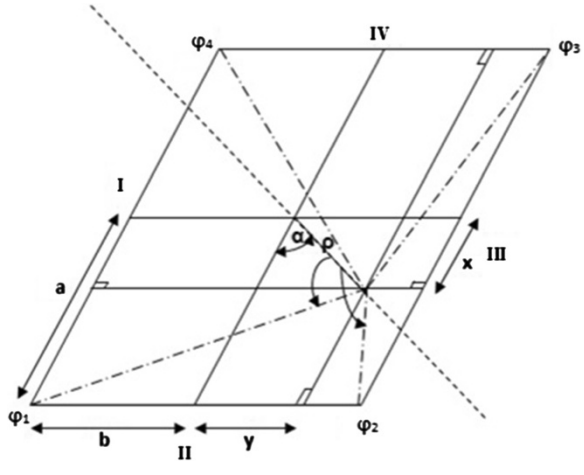

Figure 3 Schematic view for the azimuthal angle values in the bar source ($\alpha \ge \alpha_T$).

$$N_{b3} = \begin{cases} \int_0^{\rho_1} I_2(\rho \le R)\rho\,d\rho & (\rho_1 \le R) \\ \int_0^{R} I_2(\rho \le R)\rho\,d\rho + \int_R^{\rho_1} I_2(\rho > R)\rho\ d\rho & (\rho_1 > R) \end{cases} \tag{15}$$

$$N_{b4} = \begin{cases} \int_0^{\rho_2} I_2(\rho \le R)\rho\,d\rho & (\rho_2 \le R) \\ \int_0^{R} I_2(\rho \le R)\rho\,d\rho + \int_R^{\rho_2} I_2(\rho > R)\rho\,d\rho & (\rho_2 > R), \end{cases} \tag{16}$$

where

$$a = \frac{A}{2} \quad , \quad b = \frac{B}{2} \quad , \quad \alpha_T = \tan^{-1}\left(\frac{b}{a}\right)$$
$$\rho_1 = \frac{a}{\cos\alpha} \quad , \quad \rho_2 = \frac{b}{\sin\alpha}. \tag{17}$$

I_1 and I_2 are the numerator and the denominator, respectively, of $\bar{d}$ in the equation obtained by Abbas et al. [16] for non-axial point source, and h_o is the distance between the source active volume and the detector upper surface.

The new forms of the average path length traveled by the photon through the detector inactive layer and the detector end cap material are given by Equations 18 and 21, respectively.

$$\overline{\delta_{\text{lay}}} = \frac{\int_{h_o}^{H+h_o}\left(\int_0^{\alpha_T} N_{L1}\,d\alpha + \int_{\alpha_T}^{\frac{\pi}{2}} N_{L2}\,d\alpha\right)dh}{\int_{h_o}^{H+h_o}\left(\int_0^{\alpha_T} N_{b3}\,d\alpha + \int_{\alpha_T}^{\frac{\pi}{2}} N_{b4}\,d\alpha\right)dh} \tag{18}$$

with

$$N_{L1} = \begin{cases} \int_0^{\rho_1} Z_1\,\rho\,d\rho & (\rho_1 \le R) \\ \int_0^{R} Z_1\,\rho\,d\rho + \int_R^{\rho_1} Z_3\,\rho\,d\rho & (\rho_1 > R) \end{cases} \tag{19}$$

$$N_{L2} = \begin{cases} \int_0^{\rho_2} Z_1\,\rho\,d\rho & (\rho_2 \le R) \\ \int_0^{R} Z_1\,\rho\,d\rho + \int_R^{\rho_2} Z_3\,\rho\,d\rho & (\rho_2 > R), \end{cases} \tag{20}$$

where Z_1 and Z_3 are already defined in Table 2.

$$\overline{\delta_{\text{cap}}} = \frac{\int_{h_o}^{H+h_o}\left(\int_0^{\alpha_T} N_{C1}\,d\alpha + \int_{\alpha_T}^{\frac{\pi}{2}} N_{C2}\,d\alpha\right)dh}{\int_{h_o}^{H+h_o}\left(\int_0^{\alpha_T} N_{b3}\,d\alpha + \int_{\alpha_T}^{\frac{\pi}{2}} N_{b4}\,d\alpha\right)dh} \tag{21}$$

with

$$N_{C1} = \begin{cases} \int_0^{\rho_1} Z'_1\,\rho\,d\rho & (\rho_1 \le R) \\ \int_0^{R} Z'_1\,\rho\,d\rho + \int_R^{\rho_1} Z'_3\,\rho\,d\rho & (\rho_1 > R) \end{cases} \tag{22}$$

$$N_{C2} = \begin{cases} \int_0^{\rho_2} Z'_1\,\rho\,d\rho & (\rho_2 \le R) \\ \int_0^{R} Z'_1\,\rho\,d\rho + \int_R^{\rho_2} Z'_3\,\rho\,d\rho & (\rho_2 > R), \end{cases} \tag{23}$$

where Z'_1 and Z'_3 are as identified before in Table 3.

If Δh is the source container bottom thickness, Δy is the source container wall thickness from the minor axis, and Δx is the source container wall thickness from the major axis. Table 4 shows the possible path lengths traveled by the photon within the source and the source container, while Table 5 shows the values of the polar and azimuthal angles of the source; the source container also shows the maximum angle of the photon to enter the detector from the face and the minimum angle of the photon to enter the detector from the side which are labeled by $\theta_{\max}$ and $\theta_{\min}$, respectively.

The self-attenuation factor of the source matrix is given by

$$S_{\text{self}} = e^{-\mu_s \bar{t}}, \tag{24}$$

Table 4 The possible path lengths traveled by the photon within the source and the source container

	The possible path lengths	
	The source	**The source container**
To exit from the base	$t_0 = \frac{h-h_o}{\cos\theta}$	$t_{0c} = \frac{\Delta h}{\cos\theta}$
To exit from side I	$t_1 = \frac{b+y}{\sin\theta\sin\beta}$	$t_{1c} = \frac{\Delta y}{\sin\theta\sin\beta}$
To exit from side II	$t_2 = \left\lvert\frac{a-x}{\sin\theta\cos\beta}\right\rvert$	$t_{2c} = \left\lvert\frac{\Delta x}{\sin\theta\cos\beta}\right\rvert$
To exit from side III	$t_3 = \left\lvert\frac{b-y}{\sin\beta\sin\theta}\right\rvert$	$t_{3c} = t_{1c} = \frac{\Delta y}{\sin\theta\sin\beta}$
To exit from side IV	$t_4 = \frac{a+x}{\sin\theta\cos\beta}$	$t_{4c} = t_{2c} = \left\lvert\frac{\Delta x}{\sin\theta\cos\beta}\right\rvert$
	where $\beta = \alpha + \varphi \quad , \quad x = \rho\cos\alpha \quad , \quad y = \rho\sin\alpha \quad , \quad \alpha = \tan^{-1}\left(\frac{y}{x}\right)$	

Table 5 Values of the polar and the azimuthal angles of the source and the source container

The source		The source container	
The polar angles	**The azimuthal angles**	**The polar angles**	**The azimuthal angles**
$\theta_1 = \tan^{-1}\left\lvert\frac{b+y}{(h-h_o)\sin\beta}\right\rvert$	$\varphi_1 = \frac{\pi}{2} - \alpha + \tan^{-1}\left(\frac{a-x}{b+y}\right)$	$\theta_{1c} = \tan^{-1}\left\lvert\frac{b+\Delta y+y}{(h-h_o)\sin\beta}\right\rvert$	$\varphi_{1c} = \frac{\pi}{2} - \alpha + \tan^{-1}\left(\frac{a+\Delta x-x}{b+\Delta y+y}\right)$
$\theta_2 = \tan^{-1}\left\lvert\frac{a-x}{(h-h_o)\cos\beta}\right\rvert$	$\varphi_2 = \pi - \alpha + \tan^{-1}\left(\frac{b-y}{a-x}\right)$	$\theta_{2c} = \tan^{-1}\left\lvert\frac{a+\Delta x-x}{(h-h_o)\cos\beta}\right\rvert$	$\varphi_{2c} = \pi - \alpha + \tan^{-1}\left(\frac{b+\Delta y-y}{a+\Delta x-x}\right)$
$\theta_3 = \tan^{-1}\left\lvert\frac{b-y}{(h-h_o)\sin\beta}\right\rvert$	$\varphi_3 = 2\pi - \alpha - \tan^{-1}\left(\frac{b-y}{a+x}\right)$	$\theta_{3c} = \tan^{-1}\left\lvert\frac{b+\Delta y-y}{(h-h_o)\sin\beta}\right\rvert$	$\varphi_{3c} = 2\pi - \alpha - \tan^{-1}\left(\frac{b+\Delta y-y}{a+\Delta x+x}\right)$
$\theta_4 = \tan^{-1}\left\lvert\frac{a+x}{(h-h_o)\cos\beta}\right\rvert$	$\varphi_4 = \begin{cases} 2\pi - \alpha + \tan^{-1}\left(\frac{b+y}{a+x}\right) & (a \geq a_T) \\ \tan^{-1}\left(\frac{b+y}{a+x}\right) - \alpha & (a < a_T) \end{cases}$	$\theta_{4c} = \tan^{-1}\left\lvert\frac{a+\Delta x+x}{(h-h_o)\cos\beta}\right\rvert$	$\varphi_{4c} = \begin{cases} 2\pi - \alpha + \tan^{-1}\left(\frac{b+\Delta y+y}{a+\Delta x+x}\right) & (a \geq a_T) \\ \tan^{-1}\left(\frac{b+\Delta y+y}{a+\Delta x+x}\right) - \alpha & (a < a_T) \end{cases}$
$\theta_{max} = \tan^{-1}\left\lvert\frac{\rho\cos\varphi + \sqrt{R^2 - \rho^2\sin^2\varphi}}{h}\right\rvert$			
$\theta_{min} = \tan^{-1}\left\lvert\frac{\rho\cos\varphi - \sqrt{R^2 - \rho^2\sin^2\varphi}}{h+L}\right\rvert$			

where μ_s is the attenuation coefficient of the source matrix, and $\bar{t}$ is the average path length traveled by a photon inside the source and is given by

$$\bar{t} = \overline{t(t_j, \theta_i, \varphi_i)} = \frac{\int_{h_o}^{H+h_o} \left(\int_0^{\alpha_T} M_{b1}\, d\alpha + \int_{\alpha_T}^{\frac{\pi}{2}} M_{b2}\, d\alpha \right) dh}{\int_{h_o}^{H+h_o} \left(\int_0^{\alpha_T} M_{b3}\, d\alpha + \int_{\alpha_T}^{\frac{\pi}{2}} M_{b4}\, d\alpha \right) dh}, \tag{25}$$

where j takes the values from 0 to 4, while i takes the values from 1 to 4.

The values of M_{b1}, M_{b2}, M_{b3}, and M_{b4} are given as follows:

$$M_{b1} = \begin{cases} \int_0^{\rho_1} g_{b1}\rho\, d\rho & (\rho_1 \le R) \\ \int_0^{R} g_{b2}\rho\, d\rho + \int_R^{\rho_1} g_{b3}\rho\, d\rho & (\rho_1 > R) \end{cases} \tag{26}$$

$$M_{b2} = \begin{cases} \int_0^{\rho_2} g_{b1}\rho\, d\rho & (\rho_2 \le R) \\ \int_0^{R} g_{b2}\rho\, d\rho + \int_R^{\rho_2} g_{b3}\rho\, d\rho & (\rho_2 > R) \end{cases} \tag{27}$$

$$M_{b3} = \begin{cases} \int_0^{\rho_1} g_{b4}\rho\, d\rho & (\rho_1 \le R) \\ \int_0^{R} g_{b4}\rho\, d\rho + \int_R^{\rho_1} g_{b5}\rho\, d\rho & (\rho_1 > R) \end{cases} \tag{28}$$

$$M_{b4} = \begin{cases} \int_0^{\rho_2} g_{b4}\rho\, d\rho & (\rho_2 \le R) \\ \int_0^{R} g_{b4}\rho\, d\rho + \int_R^{\rho_2} g_{b5}\rho\, d\rho & (\rho_2 > R). \end{cases} \tag{29}$$

Now, we can find the values of g_{b1}, g_{b2}, g_{b3}, g_{b4}, and g_{b5} (consequently, we can find the value of $\bar{t}$), see Figures 3 and 4.

$$g_{b1} = \begin{cases} \left[\int_0^{\varphi_1} p_1 + \int_{\varphi_1}^{\varphi_2} p_2 + \int_{\varphi_2}^{\varphi_3} p_3 + \int_{\varphi_3}^{\varphi_4} p_4 + \int_{\varphi_4}^{2\pi} p_1 \right] d\varphi & (\alpha \ge \alpha_T) \\ \left[\int_0^{\varphi_4} p_4 + \int_{\varphi_4}^{\varphi_1} p_1 + \int_{\varphi_1}^{\varphi_2} p_2 + \int_{\varphi_2}^{\varphi_3} p_3 + \int_{\varphi_3}^{2\pi} p_4 \right] d\varphi & (\alpha < \alpha_T) \end{cases}, \tag{30}$$

where

$$p_1 = \begin{cases} \int_0^{\theta_{\max}} t_o \sin\theta\, d\theta & (\theta_1 \ge \theta_{\max}) \\ \left[\int_0^{\theta_1} t_o + \int_{\theta_1}^{\theta_{\max}} t_1 \right] \sin\theta\, d\theta & (\theta_{\max} > \theta_1) \end{cases} \tag{31}$$

$$p_2 = \begin{cases} \int_0^{\theta_{\max}} t_o \sin\theta\, d\theta & (\theta_2 \ge \theta_{\max}) \\ \left[\int_0^{\theta_2} t_o + \int_{\theta_2}^{\theta_{\max}} t_2 \right] \sin\theta\, d\theta & (\theta_{\max} > \theta_2) \end{cases} \tag{32}$$

$$p_3 = \begin{cases} \int_0^{\theta_{\max}} t_o \sin\theta\, d\theta & (\theta_3 \ge \theta_{\max}) \\ \left[\int_0^{\theta_3} t_o + \int_{\theta_3}^{\theta_{\max}} t_3 \right] \sin\theta\, d\theta & (\theta_{\max} > \theta_3) \end{cases} \tag{33}$$

$$p_4 = \begin{cases} \int_0^{\theta_{\max}} t_o \sin\theta d\theta & (\theta_4 \ge \theta_{\max}) \\ \left[\int_0^{\theta_4} t_o + \int_{\theta_4}^{\theta_{\max}} t_4 \right] \sin\theta\, d\theta & (\theta_{\max} > \theta_4) \end{cases} \tag{34}$$

$$g_{b2} = 2\int_0^{\pi} \int_0^{\theta_{\max}} t_o \sin\theta\, d\theta\, d\varphi \tag{35}$$

$$g_{b3} = 2\int_0^{\varphi_c} \int_{\theta_{\min}}^{\theta_{\max}} t_o \sin\theta\, d\theta\, d\varphi \tag{36}$$

$$g_{b4} = 2\int_0^{\pi} \int_0^{\theta_{\max}} \sin\theta\, d\theta\, d\varphi \tag{37}$$

$$g_{b5} = 2\int_0^{\varphi_c} \int_{\theta_{\min}}^{\theta_{\max}} \sin\theta\, d\theta\, d\varphi. \tag{38}$$

The attenuation factor of the container material is given by

$$S_{sc} = e^{-\mu_c \bar{t}_c}, \tag{39}$$

where μ_c is the attenuation coefficient of the source container material, and $\bar{t}_c$ is the average path length traveled by a photon inside the source container and is expressed as

$$\bar{t}_c = \overline{t(t_{jc}, \theta_{ic}, \varphi_{ic})}. \tag{40}$$

Experimental setup

The FEP values were measured by employing two different NaI (Tl) detectors called as Det. 1 and Det. 2. The manufacturer parameters and the setup values are shown in Table 6.

The sources used are polypropylene (PP) plastic vials of volumes 100 and 200 mL filled with an aqueous solution containing ^{152}Eu radionuclide which emits γ-ray in the energy range from 121 to 1408 keV. Table 7 shows the dimensions of the sources. The efficiency measurements are carried out by positioning the sources over the end cap of the detector. In order to minimize the dead time, the activity of the sources is prepared to be 5,048 ± 49.98 Bq. The measurements are carried out to obtain statistically significant main peaks in the spectra that are recorded and processed by winTMCA32 software made by ICx Technologies (ICx Technologies GmbH, Solingen, Germany). The acquisition time is high enough to get a number of counts at least 20,000, which makes the statistical uncertainties to be less than 0.5%. The measured spectra were analyzed with Genie 2000 software (CANBERRA Industries Inc., Meriden, CT, USA) using its automatic peak search and peak area calculations, along with changes in the peak fit using the interactive peak fit interface when necessary to reduce the residuals and error in the peak area values. The peak areas, the live time, the run time, and the start time for each spectrum are entered in the spreadsheets that are used to perform the calculations necessary to generate the efficiency curves.

Table 6 The manufacturer parameters and the setup values

Items	Det. 1	Det. 2
Manufacturer	Canberra	Canberra
Serial number	09L 654	09L 652
Detector model	802	802
Type	Cylindrical	Cylindrical
Mounting	Vertical	Vertical
Resolution (FWHM) at 662 keV	8.5%	7.5%
Cathode-to-anode voltage	+1,100 V dc	+1,100 V dc
Tube base	Model 2007	Model 2007
Shaping mode	Gaussian	Gaussian
Crystal type	NaI (Tl)	NaI (Tl)
Crystal volume (cm^3)	103	347.64

Table 7 Parameters of the sources

Items	Source volume (mL)	
	100	200
Dimension of the cross-section body (mm^2)	59.23 × 37.88	60.48 × 60.48
Height (mm)	51.02	61.4
Wall thickness (mm)	1.5	1.52
Activity (Bq)	5,048 ± 49.98	5,048 ± 49.98

The full-energy peak efficiency values for the two NaI (Tl) detectors were measured as a function of the photon energy and calculated using the following equation:

$$\varepsilon(E) = \frac{N(E)}{T\, A_S\, P(E)} \prod C_i, \tag{41}$$

where $N(E)$ is the number of counts under the full-energy peak that is determined using Genie 2000 software, T is the measuring time (in seconds), $P(E)$ is the photon emission probability at energy E, A_S is the radionuclide activity, and C_i are the correction factors due to dead time and radionuclide decay. All the sources were measured on the detector entrance window as an absorber to avoid the effect of β- and X-rays, so no correction was made for X-gamma coincidences. This is because, in most cases, the accompanying X-ray was soft enough to be absorbed completely before entering the detector and also the angular correlation effects can be negligible for the low source-to-detector distance. It must be noted that gamma-gamma coincidences were not taken into account, which can induce deviations of the peaks' area. In these measurements of low activity sources, the dead time is always less than 3%. So, the corresponding factor is obtained simply using the ADC live time. The statistical uncertainties of the net peak areas are smaller than 0.5% since the acquisition time is long enough to get a number of counts of at least 20,000. The background subtraction is done. The decay correction C_d for the calibration source from the reference time to the run time is given by

$$C_d = e^{\lambda\, \Delta T}, \tag{42}$$

where λ is the decay constant, and ΔT is the time interval over which the source decays corresponding to the run time. The main source of uncertainty in the

efficiency calculations is the uncertainties of the activities of the standard source solutions. Once the efficiencies have been fixed by applying the correction factors, the overall efficiency curve is obtained by fitting the experimental points to a polynomial logarithmic function of the fifth order using a nonlinear least square fit. In this way, the correlation between the data points from the same calibrated source has been included to avoid the overestimation of the uncertainty in the measured efficiency. The uncertainty in the full-energy peak efficiency σ_ε is given by

$$\sigma_\varepsilon = \varepsilon \sqrt{\left(\frac{\partial \varepsilon}{\partial A}\right)^2 \sigma_A{}^2 + \left(\frac{\partial \varepsilon}{\partial P}\right)^2 \sigma_P{}^2 + \left(\frac{\partial \varepsilon}{\partial N}\right)^2 \sigma_N{}^2}, \tag{43}$$

where σ_A, σ_P, and σ_N are the uncertainties associated with the quantities A_S, $P(E)$, and $N(E)$, respectively.

Results and discussion

Figures 5 and 6 show the full-energy peak efficiencies for both NaI (Tl) detectors (Det. 1 and Det. 2) which include measured, calculated with S_{self}, and calculated without S_{self} for parallelepiped sources (100 and 200 mL) placed at the end cap of the detector as functions of the photon energy. The percentage deviations between the calculated (with and without S_{self}) and the measured full-energy peak efficiency values are calculated by

$$\Delta_1\ \% = \frac{\varepsilon_{\text{cal-with } S_{self}} - \varepsilon_{meas}}{\varepsilon_{\text{cal-with } S_{self}}} \times 100 \tag{44}$$

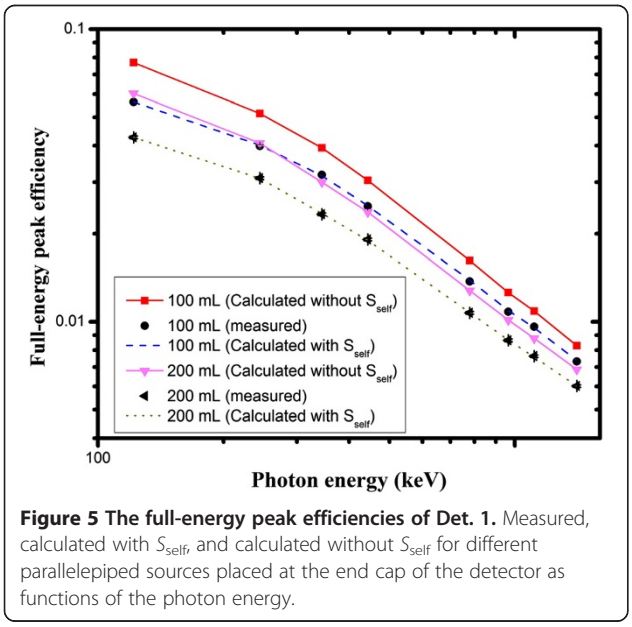

Figure 5 The full-energy peak efficiencies of Det. 1. Measured, calculated with S_{self}, and calculated without S_{self} for different parallelepiped sources placed at the end cap of the detector as functions of the photon energy.

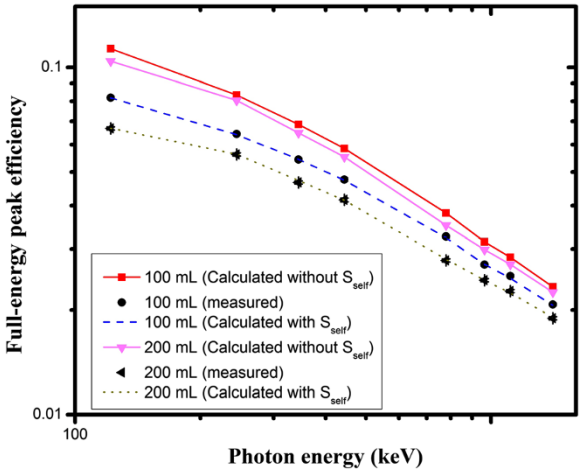

Figure 6 The full-energy peak efficiencies of Det. 2. Measured, calculated with S_{self}, and calculated without S_{self} for different parallelepiped sources placed at the end cap of the detector as functions of the photon energy.

$$\Delta_2\ \% = \frac{\varepsilon_{\text{cal-without } S_{self}} - \varepsilon_{meas}}{\varepsilon_{\text{cal-without } S_{self}}} \times 100, \tag{45}$$

where $\varepsilon_{\text{cal-with } Sself}$, $\varepsilon_{\text{cal-without } Sself}$, and ε_{meas} are the calculated with/without self-attenuation factor and experimentally measured efficiencies, respectively. Table 8 shows the

Table 8 Comparison between Δ_1% and Δ_2% for sources placed at the end cap of the detectors

Detector	Energy (keV)	Source volume (mL)			
		100		200	
		Δ_1%	Δ_2%	Δ_1%	Δ_2%
Det. 1	121.78	0.04	26.54	−0.01	29.18
	244.69	0.59	22.51	−0.25	24.17
	344.28	−0.61	19.23	0.72	22.39
	443.97	0.46	18.51	−0.79	19.45
	778.90	0.72	15.06	0.22	16.22
	964.13	1.00	14.02	0.25	14.83
	1,112.11	−0.85	11.58	−0.55	13.24
	1,408.01	0.85	11.76	0.05	12.28
Det. 2	121.78	−0.10	27.71	0.09	35.87
	244.69	−0.41	22.83	0.10	30.21
	344.28	0.13	20.82	1.36	28.11
	443.97	−0.41	18.73	−0.24	24.85
	778.90	−1.00	14.35	0.86	20.80
	964.13	0.25	14.06	−0.02	18.36
	1,112.11	−1.42	11.75	−1.19	16.28
	1,408.01	−0.65	11.01	0.51	15.88

comparison between the percentage deviations $\Delta_1\%$ and $\Delta_2\%$ for the different volumes placed at the end cap of the NaI (Tl) detectors. The discrepancies between the calculated with S_{self} and measured values were found to be less than (2%), while those between calculated without S_{self} and measured values were found to be less than (35%). Obviously, the non-inclusion of the self-attenuation factor in the calculations caused an increase in the full-energy peak efficiency values. So, to get correct results, the self-attenuation factor must be taken into consideration. Also, Figures 5 and 6, and Table 8 show that the source of self-attenuation is more effective with large sources, where the photon has traveled a larger distance within a source matrix, so the possibility of getting it absorbed will be more; hence, the attenuation will be more. Its effect starts to decrease when the volume decreases (the distance traveled by the photon within the source matrix decreases).

Conclusions

In the present work, the authors introduced separate calculation of the factors related to photon attenuation in the detector end cap, inactive layer, source container, and the self-attenuation of the source matrix. Also, a direct analytical approach for calculating the full-energy peak efficiency has been derived. The examination of the present results as given in the figures reflects the importance of considering the self-attenuation factor in studying the efficiency of any detector using parallelepiped sources.

Competing interests

The authors declare that they have no competing interests.

Authors' contributions

The mathematical theoretical analysis was carried out by MMG, AME-K, and NNM. The experimental works were carried out by MSB and MMG. All authors analyzed and discussed the results. The manuscript was written by MSB and SIJ, and the figures were prepared by MSB, EAE-M, SSN, and ADD. All authors read and approved the final manuscript.

Acknowledgements

The authors would like to express their sincere thanks to Prof. Dr. Mahmoud I. Abbas, Faculty of Science, Alexandria University, for the very valuable professional guidance in the area of radiation physics and for his fruitful scientific collaborations on this topic. Dr. Mohamed S. Badawi would like to introduce a special thanks to The Physikalisch-Technische Bundesanstalt (PTB) in Braunschweig, Berlin, Germany for fruitful help in preparing the homemade volumetric sources.

Author details

[1]Physics Department, Faculty of Science, Alexandria University, Alexandria 21511, Egypt. [2]Department of Physics, Faculty of Mathematics and Natural Sciences, University of Montenegro, Cetinjski put b.b, Podgorica 81000, Montenegro. [3]Centre for Nuclear Competence and Knowledge Management, University of Montenegro, Dz. Vasingtona bb, MNE-2000, Podgorica 81000, Montenegro. [4]Department of Mathematics, Maritime Faculty, University of Montenegro, Kotor, Montenegro.

Received: 26 July 2013 Accepted: 23 September 2013
Published: 30 September 2013

References

1. Yalcin, S, Gurler, O, Kaynak, G, Gundogdu, O: Calculation of total counting efficiency of a NaI(Tl) detector by hybrid Monte-Carlo method for point and disk sources. Appl. Radiat. Isot. **65**, 1179–1186 (2007)
2. Vargas, MJ, Timón, AF, Díaz, NC, Sánchez, DP: Monte Carlo simulation of the self-absorption corrections for natural samples in gamma-ray spectrometry. Appl. Radiat. Isot. **57**, 893–898 (2002)
3. Korun, M: Measurement of the average path length of gamma-rays in samples using scattered radiation. Appl. Radiat. Isot. **56**, 77–83 (2002)
4. Lippert, J: Detector-efficiency calculation based on point-source measurement. Appl. Radiat. Isot. **34**, 1097–110 (1983)
5. Haase, G, Tait, D, Wiechon, A: Application of new Monte Carl method for determination of summation and self-attenuation corrections in gamma spectrometry. Nucl. Instrum. Methods A **336**, 206–214 (1993)
6. Moens, L, Hoste, J: Calculation of the peak efficiency of high-purity germanium detectors. Appl. Radiat. Isot. **34**, 1085–1095 (1983)
7. Sima, O, Arnold, D: Self-attenuation and coincidence summing corrections calculated by Monte Carlo simulations for gamma-spectrometric measurements with well-type germanium detectors. Appl. Radiat. Isot. **47**, 889–893 (1996)
8. Wang, TK, Mar, WY, Ying, TH, Liao, CH, Tseng, CL: HPGe detector absolute-peak-efficiency calibration by using the ESOLAN program. Appl. Radiat. Isot. **46**, 933–944 (1995)
9. Wang, TK, Mar, WY, Ying, TH, Tseng, CH, Liao, CH, Wang, MY: HPGe detector efficiency calibration for extended cylinder and marinelli-beaker sources using the ESOLAN program. Appl. Radiat. Isot. **48**, 83–95 (1997)
10. Selim, YS, Abbas, MI, Fawzy, MA: Analytical calculation of the efficiencies of gamma scintillators. Part I: total efficiency of coaxial disk sources. Radiat. Phys. Chem **53**, 589–592 (1998)
11. Selim, YS, Abbas, MI: Analytical calculations of gamma scintillators efficiencies. Part II: total efficiency for wide coaxial disk sources. Radiat. Phys. Chem **58**, 15–19 (2000)
12. Abbas, MI: A direct mathematical method to calculate the efficiencies of a parallelepiped detector for an arbitrarily positioned point source. Radiat. Phys. Chem. **60**, 3–9 (2001)
13. Abbas, MI: Analytical formulae for well-type NaI(Tl) and HPGe detectors efficiency computation. Appl. Radiat. Isot. **55**, 245–252 (2001)
14. Abbas, MI, Selim, YS: Calculation of relative full-energy peak efficiencies of well-type detectors. Nucl. Instrum. Methods A **480**, 651–657 (2002)
15. Abbas, MI: HPGe detector absolute full-energy peak efficiency calibration including coincidence correction for circular disc sources. J. Phys. D Appl. Phys. **39**, 3952–3958 (2006)
16. Abbas, MI, Nafee, SS, Selim, YS: Calibration of cylindrical detectors using a simplified theoretical approach. Appl. Radiat. Isot. **64**, 1057–1064 (2006)
17. Pibida, L, Nafee, SS, Unterweger, M, Hammond, MM, Karam, L, Abbas, MI: Calibration of HPGe gamma-ray detectors for measurement of radio-active noble gas sources. Appl. Radiat. Isot. **65**, 225–233 (2007)
18. Nafee, SS, Abbas, MI: Calibration of closed-end HPGe detectors using bar (parallelepiped) sources. Nucl. Instrum. Methods A **592**, 80–87 (2008)
19. Badawi, MS, Gouda, MM, Nafee, SS, El-Khatib, AM, El-Mallah, EA: New algorithm for studying the effect of self attenuation factor on the efficiency of γ-rays detectors. Nucl. Instrum. Methods A **696**, 164–170 (2012)
20. Badawi, MS, Gouda, MM, Nafee, SS, El-Khatib, AM, El-Mallah, EA: New analytical approach to calibrate the co-axial HPGe detectors including correction for source matrix self-attenuation. Appl. Radiat. Isot. **70**, 2661–2668 (2012)
21. El-Khatib, AM, Gouda, MM, Badawi, MS, Nafee, SS, El-Mallah, EA: New analytical approach to calibrate the NaI (Tl) detectors using spherical radioactive sources. Radiat. Prot. Dosimetry **156**(1), 109–117 (2013). doi:10.1093/rpd/nct048

doi:10.1186/2251-7235-7-52
Cite this article as: El-Khatib *et al.*: **Calculation of full-energy peak efficiency of NaI (Tl) detectors by new analytical approach for parallelepiped sources.** *Journal of Theoretical and Applied Physics* 2013 **7**:52.